AIAA JOURNAL
Vol. 34, No. 8, August 1996

Central and Noncentral Normal Impact on Orthotropic Composite Cylindrical Shells

S. W. Gong,* V. P. W. Shim,† and S. L. Toh†
National University of Singapore, 119260 Singapore

The response of orthotropic composite cylindrical shells subjected to low-velocity impact by a solid striker is described. An analytical solution that accommodates normal impact at any location is presented. This solution is based on a higher order shear deformation theory and derived in terms of two sets of shell coordinates and an integer factor to facilitate analysis of noncentral impact. An analytic impact force function recently proposed by the authors is used to predict the contact force between striker and shell and this is incorporated into the solution. Impact experiments are also conducted on a simply supported glass/epoxy cylindrical shell. The effective contact stiffness between the shell and striker is obtained by fitting an impact force function to experimental data. The strain responses of the shell to central and noncentral impact are investigated and the present solutions verified by the experiments.

Nomenclature

$A_{ij}, B_{ij}, D_{ij}, E_{ij}, F_{ij}, H_{ij}$	= laminate stiffness constants defined in Eq. (A2)
F	= impact force
K_1	= equivalent stiffness of a simply supported shell
K_2	= contact stiffness
K_2^*	= effective contact stiffness
L, R, h	= length, radius, and thickness of a cylindrical shell
m_1	= mass of shell
m_1^*	= effective mass of shell
m_2	= impact mass
$Q_{ij}^{(k)}$	= transformed stiffness constants in a shell coordinate system
T	= contact duration
t	= time
u, v, w	= displacements along the x, θ, and z axes
V	= impact velocity
X, Θ, Z	= absolute orthogonal curvilinear coordinates for cylindrical shell
x, θ, z	= relative orthogonal curvilinear coordinates for cylindrical shell
β_1, β_2	= bending slopes in the α_1–ζ and α_2–ζ planes
ε_i	= strain components
ω_{mn}	= frequency of mode mn
ξ^*	= integer factor defined in Eq. (7)

I. Introduction

WITH the increased use of fibrous composites in aerospace applications, the subject of impact on composite structures has received widespread attention in recent years. Sun and Chattopadhyay[1] and Dobyns[2] used the first-order shear deformation theory (FSDT) developed by Whitney and Pagano[3] to analyze a simply supported, specially orthotropic plate subjected to central point impact. Ramkumar and Thakar[4] employed Donnell's equations based on classical shell theory (CST) to study cylindrical thin shells and presented the low-velocity impact response of cylindrical laminated shells of large radii. They assumed that impact force varies linearly with time and followed Sun and Chattopadhyay's and Dobyns' procedure to determine the response.[1,2] Christoforou and Swanson[5] used the FSDT developed by Bert and Birman[6] for cylindrical shells to examine simply supported orthotropic cylindrical shells subjected to impact and presented an analytic solution to the problem. In their solution, the deceleration of the impacting mass was used to estimate the impact force, and local contact deformation between the striker and shell during impact was neglected. Validity of their solution was confined to response during contact between the impactor and shell. Gong et al.[7] adopted Christoforou and Swanson's procedure and undertook an analysis of laminated open cylindrical shells under impact loading. In their analysis, contact deformation was considered and an analytic function to describe it was proposed and incorporated into the analysis. Recently, Gong et al.[8] presented a set of solutions for prediction of the displacement and stress responses of composite laminated shells subjected to low-velocity impact. These solutions are based on a higher order shear deformation theory (HSDT) and are applicable to laminated composites in the form of flat plates, cylindrical shells, and spherical shells subjected to impact. The solutions also facilitate study of the dynamic response of shells excited by impact for a total time history ($0 < t < +\infty$).

However, all of the preceding studies listed are restricted to composite plates or shells subjected to impact at their center. The problem of composite shells subjected to noncentral impact appears not to have been addressed. This work presents an analysis that accommodates noncentral impact on shells. Solutions are derived in terms of two sets of shell coordinates—(x, θ, z) and (X, Θ, Z), as shown in Fig. 1—and an integer factor defined in Eq. (7). The HSDT developed by Reddy and Liu[9] is employed in this analysis. Present solutions were verified by impact experiments on a simply supported glass/epoxy ogival shell and are suitable for the study of the transient dynamic response of composite laminated cylindrical shells impacted by a solid striker at any location.

II. Solution for Cylindrical Shells Subjected to Impact

Consider the closed composite cylindrical shell in Fig. 1 impacted at an arbitrary location by a solid striker. The shell has a mean radius R, length L, and thickness h and is simply supported at its two ends. Two coordinate systems, (x, θ, z) and (X, Θ, Z), are employed to describe the impacted shell, with the sign convention for displacements and stresses depicted in Fig. 1. The impact point is a distance L_1 ($L_1 < L/2$) from one end of the cylinder and $L_2 = L - L_1$ (Fig. 1). The relationship between the two coordinate systems is

$$X = x + [(L/2) - L_1]; \qquad \Theta = \theta; \qquad Z = z \tag{1}$$

The equations of motion developed by Reddy and Liu[9] for a shell subjected to a distributed transverse load q_n can be expressed in terms of deflections and rotations[10]:

$$[L_{ij}]\{u, v, w, \beta_1, \beta_2\}^T = \{0, 0, (\rho h \ddot{w} - q_n); 0, 0\}^T \tag{2}$$

Received March 20, 1995; revision received Aug. 22, 1995; accepted for publication Nov. 16, 1995. Copyright © 1996 by the authors. Published by the American Institute of Aeronautics and Astronautics, Inc., with permission.

*Research Scholar, Department of Mechanical and Production Engineering.
†Senior Lecturer, Department of Mechanical and Production Engineering.

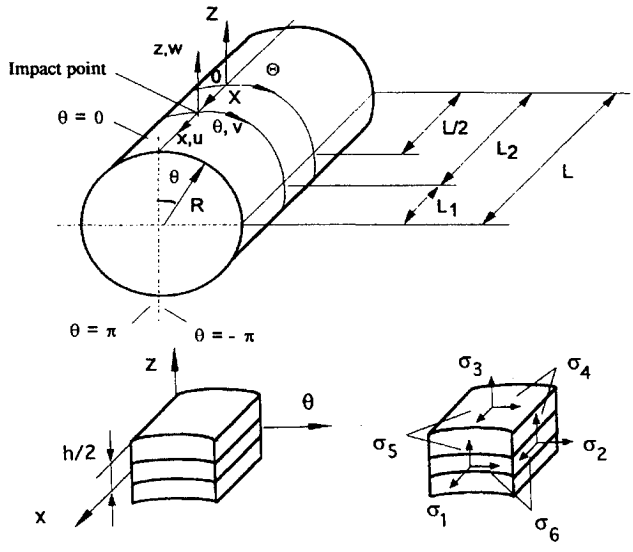

Fig. 1 Shell geometry, coordinate systems used, and sign convention for displacements and stresses.

where [ ] and { } represent matrices and vectors, respectively, and the differential operators L_{ij} are given in the Appendix.

Navier solutions are employed to solve Eq. (2); these solutions are restricted to crossply laminated shells because they exist if the following stiffnesses are zero[9]:

$$A_{i6} = B_{i6} = D_{i6} = E_{i6} = F_{i6} = H_{i6} = 0 \qquad (i = 1, 2)$$

$$A_{45} = D_{45} = F_{45} = 0 \; A_{45} = D_{45} = F_{45} = 0 \tag{3}$$

The simply supported boundary conditions are

$$v(L_1, \theta) = w(L_1, \theta) = N_1(L_1, \theta) = M_1(L_1, \theta)$$

$$= P_1(L_1, \theta) = \beta_\theta(L_1, \theta) = 0 \tag{4a}$$

$$v(-L_2, \theta) = w(-L_2, \theta) = N_1(-L_2, \theta)$$

$$= M_1(-L_2, \theta) = P_1(-L_2, \theta) = \beta_\theta(-L_2, \theta) = 0 \tag{4b}$$

For a given distributed dynamic load $q_n(x, \theta, t)$, solutions to Eq. (2) that satisfy the boundary conditions (4a) and (4b) can be separated into functions of time and position as follows:

$$w(x, \theta, t) = \sum_{m=1}^{\infty}\sum_{n=1}^{\infty} W_{mn}(t)\cos\frac{m\xi^*\pi x}{L}\cos n\theta \tag{5a}$$

$$u(x, \theta, t) = \sum_{m=1}^{\infty}\sum_{n=1}^{\infty} U_{mn}(t)\sin\frac{m\xi^*\pi x}{L}\cos n\theta \tag{5b}$$

$$v(x, \theta, t) = \sum_{m=1}^{\infty}\sum_{n=1}^{\infty} V_{mn}(t)\cos\frac{m\xi^*\pi x}{L}\sin n\theta \tag{5c}$$

$$\beta_1(x, \theta, t) = \sum_{m=1}^{\infty}\sum_{n=1}^{\infty} X_{mn}(t)\sin\frac{m\xi^*\pi x}{L}\cos n\theta \tag{5d}$$

$$\beta_2(x, \theta, t) = \sum_{m=1}^{\infty}\sum_{n=1}^{\infty} Y_{mn}(t)\cos\frac{m\xi^*\pi x}{L}\sin n\theta \tag{5e}$$

where $m = 1, 3, 5, \ldots$, and $n = 1, 3, 5, \ldots$.

The load $q_n(x, \theta, t)$ is expressed as

$$q_n(x, \theta, t) = \sum_{m=1}^{\infty}\sum_{n=1}^{\infty} Q_{mn}(t)\cos\frac{m\xi^*\pi x}{L}\cos n\theta \tag{6}$$

In Eqs. (5a–5e) and (6), ξ^* is an integer factor defined by

$$\xi^* = [L/2L_1]^* \tag{7}$$

where $[\,]^*$ represents a function that assumes the value of the integer closest to $L/2L_1$. This function is used in the Navier solutions (5a–5e) to satisfy the boundary conditions (4a) and (4b). Note from Eq. (7) that for $L_1 = L/2i$

$$L_1 = L/2\xi^* \tag{8a}$$

$$L_2 = \frac{2\xi^* - 1}{2\xi^*}L \tag{8b}$$

and for $L_1 \neq L/2i$

$$L_1 \approx L/2\xi^* \tag{8c}$$

$$L_2 \approx \frac{2\xi^* - 1}{2\xi^*}L \tag{8d}$$

where $i = 1, 2, 3, \ldots$.

With respect to Eqs. (8a–8d), the solutions (5a–5e) satisfy the boundary conditions (4a) and (4b) exactly for $L_1 = L/2i$ ($i = 1, 2, 3, \ldots$), whereas they satisfy the boundary conditions only approximately for $L_1 \neq L/2i$.

For an impact force $F(t)$ at the point $x = \theta = 0$, $Q_{mn}(t)$ is given by[10]

$$Q_{mn}(t) \approx \frac{2F(t)}{L\pi R} \tag{9}$$

where $m = 1, 3, 5, \ldots$, and $n = 1, 3, 5, \ldots$.

Substitution of Eqs. (5a–5e) and (6) into Eq. (2) and neglecting in-surface and rotary inertia yield the following equations:

$$[T_{ij}]\{U_{mn}, V_{mn}, W_{mn}, X_{mn}, Y_{mn}\}^T$$

$$= \{0, 0, [\rho h\ddot{W}_{mn}(t) - Q_{mn}(t)], 0, 0\}^T \tag{10}$$

where T_{ij} are the constant coefficients listed in the Appendix.

Equation (10) can be reduced to a single linear second-order differential equation:

$$\ddot{W}_{mn}(t) + \omega_{mn}^2 W_{mn}(t) = \frac{Q_{mn}(t)}{\rho h} \tag{11}$$

where

$$\omega_{mn}^2 = -\frac{1}{K_{mn}\rho h} \tag{12}$$

and

$$K_{mn} = \tilde{T}_{33}/\det T \tag{13}$$

where $\tilde{T}_{33}$ is the cofactor of element T_{33} in $\det T$.

Also, from Eq. (10), the following transformations yield

$$\begin{aligned} U_{mn}(t) &= K_u W_{mn}(t) & V_{mn}(t) &= K_v W_{mn}(t) \\ X_{mn}(t) &= K_x W_{mn}(t) & Y_{mn}(t) &= K_y W_{mn}(t) \end{aligned} \tag{14}$$

where the coefficients K_u, K_v, K_x, and K_y are given by

$$\begin{aligned} K_u &= \tilde{T}_{31}/\tilde{T}_{33} & K_v &= \tilde{T}_{32}/\tilde{T}_{33} \\ K_x &= \tilde{T}_{34}/\tilde{T}_{33} & K_y &= \tilde{T}_{35}/\tilde{T}_{33} \end{aligned} \tag{15}$$

and $\tilde{T}_{ij}$ are cofactors of the element T_{ij} in $\det T$.

For zero initial displacement and velocity of the shell, the solution to Eq. (11) is

$$W_{mn}(t) = \frac{1}{\omega_{mn}\rho h}\int_0^t Q_{mn}(\tau)\sin[w_{mn}(t-\tau)]\,d\tau \tag{16}$$

Substituting Eq. (9) into Eq. (16) results in

$$W_{mn}(t) = \frac{4}{\omega_{mn}m_1}\int_0^t F(\tau)[\sin\omega_{mn}(t-\tau)]\,d\tau \tag{17}$$

The impact force function[7]

$$F(t) = \begin{cases} K_2^*[a_1(c_1-1)\sin(\omega_1 t) \\ \quad + a_2(c_2-1)\sin(\omega_2 t)] & 0 < t < T \\ 0 & t > T \end{cases} \tag{18}$$

is substituted into Eq. (17) and integrated to yield

$$W_{mn}(t) = \frac{4K_2^*}{\omega_{mn} m_1}\left[\frac{a_1(c_1-1)}{\omega_1^2-\omega_{mn}^2}(\omega_1 \sin\omega_{mn}t - \omega_{mn}\sin\omega_1 t) + \frac{a_2(c_2-1)}{\omega_2^2-\omega_{mn}^2}(\omega_2 \sin\omega_{mn}t - \omega_{mn}\sin\omega_2 t)\right] \quad 0 < t < T \tag{19a}$$

$$W_{mn}(t) = \frac{4K_2^*}{\omega_{mn} m_1}\left\{\frac{a_1(c_1-1)}{\omega_1^2-\omega_{mn}^2}[\omega_1 \sin\omega_{mn}t - \omega_1\cos\omega_1 T \sin\omega_{mn}(t-T) - \omega_{mn}\sin\omega_1 T\cos\omega_{mn}(t-T)] + \frac{a_2(c_2-1)}{\omega_2^2-\omega_{mn}^2}[\omega_2\sin\omega_{mn}t - \omega_2\cos\omega_2 T\sin\omega_{mn}(t-T) - \omega_{mn}\sin\omega_2 T\cos\omega_{mn}(t-T)]\right\} \quad t > T \tag{19b}$$

where

$$\omega_{1,2}^2 = \frac{1}{2}\left(\frac{K_1+K_2^*}{m_1^*}+\frac{K_2^*}{m_2}\right) \mp \sqrt{\frac{1}{4}\left(\frac{K_1+K_2^*}{m_1^*}-\frac{K_2^*}{m_2}\right)^2 + \frac{K_2^{*2}}{m_1^* m_2}}$$

$$c_1 = \frac{K_2^*}{K_2^* - \omega_1^2 m_2} \qquad c_2 = \frac{K_2^*}{K_2^* - \omega_2^2 m_2}$$
$$a_1 = \frac{V}{\omega_1(c_2-c_1)} \qquad a_2 = \frac{V}{\omega_2(c_1-c_2)} \tag{20}$$

Use of Eqs. (5a–5e) with the equations for strains in terms of deflections and rotations from Ref. 9, in conjunction with Eqs. (1) and (14), results in expressions for the strains generated by impact in the (X, Θ, Z) coordinate system:

$$\varepsilon_1 = \sum_{m=1}^{\infty}\sum_{n=1}^{\infty}\left[K_u + zK_x - \frac{4z^3}{3h^2}\left(K_x - \frac{m\xi^*\pi}{L}\right)\right]\frac{m\xi^*\pi}{L} \times W_{mn}(t)\cos\left\{\frac{m\xi^*\pi}{L}\left[X - \left(\frac{L}{2}-L_1\right)\right]\right\}\cos n\Theta \tag{21a}$$

$$\varepsilon_2 = \sum_{m=1}^{\infty}\sum_{n=1}^{\infty}\left[K_v + \frac{1}{n} + zK_y - \frac{4z^3}{3h^2}\left(K_y - \frac{n}{R}\right)\right] \times \frac{n}{R}W_{mn}(t)\cos\left\{\frac{m\xi^*\pi}{L}\left[X - \left(\frac{L}{2}-L_1\right)\right]\right\}\cos n\Theta \tag{21b}$$

$$\varepsilon_3 = 0 \tag{21c}$$

$$\varepsilon_4 = \sum_{m=1}^{\infty}\sum_{n=1}^{\infty}\left[K_x - \frac{m\xi^*\pi}{L} - \frac{4z^2}{h^2}\left(K_x - \frac{m\xi^*\pi}{L}\right)\right] \times W_{mn}(t)\sin\left\{\frac{m\xi^*\pi}{L}\left[X - \left(\frac{L}{2}-L_1\right)\right]\right\}\cos n\Theta \tag{21d}$$

$$\varepsilon_5 = \sum_{m=1}^{\infty}\sum_{n=1}^{\infty}\left[K_y - \frac{n}{R} - \frac{4z^2}{h^2}\left(K_y - \frac{n}{R}\right)\right] \times W_{mn}(t)\cos\left\{\frac{m\xi^*\pi}{L}\left[X - \left(\frac{L}{2}-L_1\right)\right]\right\}\sin n\Theta \tag{21e}$$

$$\varepsilon_6 = \sum_{m=1}^{\infty}\sum_{n=1}^{\infty}\left[-\frac{m\xi^*\pi}{L}K_v - \frac{n}{R}K_u - z\left(\frac{m\xi^*\pi}{L}K_y + \frac{n}{R}K_x\right) + \frac{4z^3}{3h^2}\left(\frac{m\xi^*\pi}{L}K_y + \frac{n}{R}K_x - 2\frac{m\xi^*\pi}{L}\frac{n}{R}\right)\right] \times W_{mn}(t)\sin\left\{\frac{m\xi^*\pi}{L}\left[X - \left(\frac{L}{2}-L_1\right)\right]\right\}\sin n\Theta \tag{21f}$$

III. Impact Experiments

Impact experiments were conducted on a $[0_8]$ glass/epoxy cylindrical shell with a mean radius of 0.108 m, a length of 0.28 m, and a thickness of 2.3 mm. The shell was fabricated using filament winding, and its mechanical properties were measured according to the American Society for Testing and Materials standard D3039-76[11]; the values obtained are $E_1 = 14.51$ GPa, $E_2 = 5.36$ GPa, $G_{12} = 2.51$ GPa, $\nu_{12} = 0.231$, and $\rho = 1901.5$ kg/m^2.

Figure 2 shows a schematic diagram of the experimental arrangement. A pendulum impact device was designed to allow a striker to impact shell specimens at specified velocities. The impact force was measured by a force transducer attached to a removable steel block at the tip of the pendulum rod. This block could be changed to vary the impacting mass. The transducer had a removable cap that made direct contact with the target during impact and this could be changed to alter the contact stiffness. Strains induced in the cylindrical shell were obtained from two-axis rosette gauges bonded on its inner surface. Gauges were mounted at points A′, B′, C′, D′, and E′ (behind points A, B, C, D, and E) as shown in Fig. 3. The 1 and 2 directions of the gauges coincide, respectively, with the axial and circumferential directions of the cylindrical shell, and signals from the gauges were amplified by a dynamic strain meter. Both amplified force and strain outputs were captured on a digital storage oscilloscope and the data transferred to a personal computer for subsequent processing and analysis.

The effective contact stiffness between the striker and shell was determined by fitting the impact force function (18) into experimen-

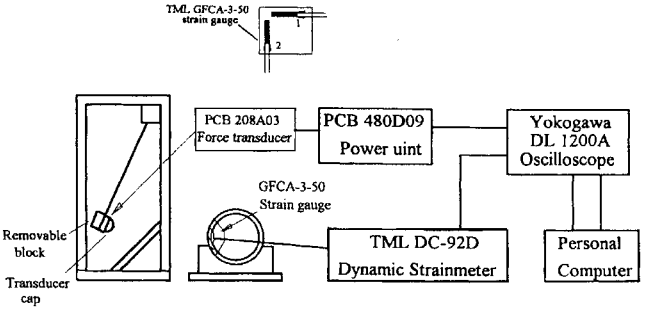

Fig. 2 Schematic diagram of impact testing arrangement.

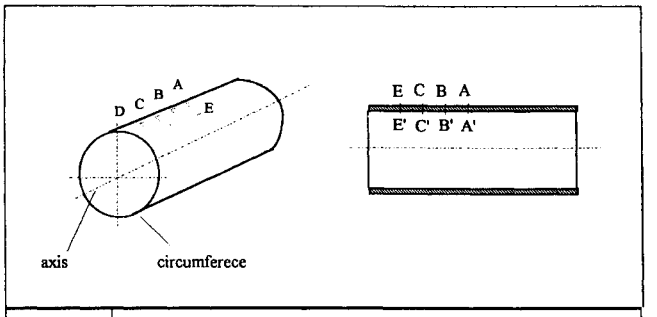

Point	A'	B'	C'	D'	E'
X (mm)	0	30	60	90	0
Θ (degree)	0	0	0	0	30
Z (mm)	-h/2	-h/2	-h/2	-h/2	-h/2

Fig. 3 Locations of impact points and strain gauges.

tal contact force–time data. The center of the shell (point A in Fig. 3) was struck by a mass of 0.075 kg at an impact velocity of 1 m/s. Contact force during impact was captured by the force transducer attached to the striker. Except for the effective contact stiffness K_2^*, the other parameters in the impact force function (18) are known; m_1^* is determined from $m_1^* = \rho h \iint_S W^2(x,\theta)\,dS$[10], in which dS is the differential surface area of the shell, whereas S is the total area, and $W(x,\theta)$ is a function of position that defines the shape of the natural mode of shell vibration. The term K_1 is determined from $K_1 = \omega_{11}^2 m_1^*$, and m_2 and V are the impact mass and impact velocity of the striker. A trial stiffness $(K_2^*)_{t1}$ is assumed for an initial calculation of the impact force. By comparing calculated values of the maximum impact force $F_{\max}$ and contact duration T with those from impact tests, $(K_2^*)_{t1}$ is adjusted to a second trial value $(K_2^*)_{t2}$ and substituted into the impact force function (18) again. This process of comparison and modification is repeated until the difference between calculated and experimental values of the maximum impact force $F_{\max}$ and contact duration T fall within 5%; i.e., the effective contact stiffness is then

$$K_2^* = \left(K_2^*\right)_{tn} \tag{22}$$

A value of 235 kN/m was obtained for K_2^*. Since earlier studies[12] on impact of spheres have shown that contact stiffness is governed by their material properties (Young's modulus) and radii, estimation of contact stiffness by central impact is sufficiently representative for impact at other locations.

IV. Analysis of Dynamic Strain Response

Strain responses of a simply supported $[0_8]$ glass/epoxy cylindrical shell subjected to central and noncentral impact were investigated. A 0.075-kg impact mass and an impact velocity of 1 m/s were used. Transient strain responses excited by impact were measured using the experimental setup shown in Fig. 2 and compared with calculations based on Eqs. (21a–21f). In the present study, strains are represented by ε_{ijk}, where the first subscript denotes the direction of strain, the second the location of the gauge, and the third the impact location.

A. Strain Response to Central Impact

A simply supported glass/epoxy composite cylinder was first subjected to impact at its center (point A in Fig. 3). The calculated and measured contact forces between the cylinder and striker are illustrated in Fig. 4. A comparison between calculated and measured values shows that the calculated contact duration and peak force differ from measured values by 5% at most; also, the calculated force–time curve matches the measured one reasonably well. This verifies that the impact force function (18) can be used to predict contact force between a striker and shell during impact.

Figures 5–7 show calculated and measured strain histories at points A′, B′, and E′ (Fig. 3). It is observed that, in general, the calculated and measured results agree. The strain histories at point A′ (behind the impact point) shown in Fig. 5 are examined in relation to the contact force (Fig. 4); the contact duration T is about 1.8 ms, and the peak force occurs at approximately $t = T/2$. During contact ($0 < t < T$), longitudinal and circumferential strains vary proportionately with contact force, increasing during loading ($0 < t < T/2$) and decreasing thereafter ($T/2 < t < T$). Maximum values occur at $t \approx T/2$, when the contact force reaches its peak. This indicates that during contact ($0 < t < T$) strain magnitudes are essentially governed by the contact force. After separation of the striker from the shell, the strains decay rapidly as the shell undergoes free vibration. The largest longitudinal strain induced after loss of contact ($t > T$) is about one-sixth the maximum value during contact, whereas the largest circumferential strain following loss of contact is only about one-ninth the maximum value during contact. Hence, the maximum strains generated occur during contact. This result shows that the contact force history and its relation to strain magnitudes should be monitored to determine the occurrence of maximum strains in an impacted shell.

The strain responses at points B′ and E′ (in the vicinity of the impact point) are shown in Figs. 6 and 7. These strain responses exhibit behavior similar to the strain response at point A′ (behind the impact point). The strain magnitudes also increase during loading and decrease as the shell is unloaded, with maximum values occurring at $t \approx T/2$. This indicates that strains around the impact point are also governed by the contact force. Figures 6 and 7 show that the maximum strain induced during impact decreases sharply with distance from the point of impact. The maximum longitudinal strain at point B′ (30 mm from A′) is only 47% of the maximum longitudinal strain at point A′, whereas the maximum circumferential strain at point E′ reduces to 36% of the maximum circumferential strain at point A′. It is therefore evident that maximum normal strains occur at the impact point.

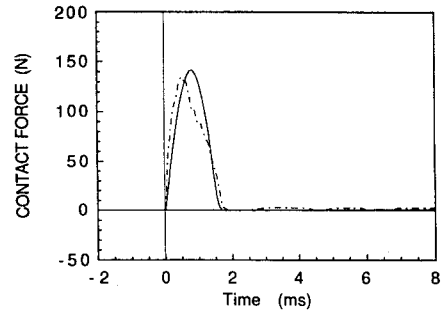

Fig. 4 Contact force between striker and cylindrical shell: –·–·–, experiment and ——, theory.

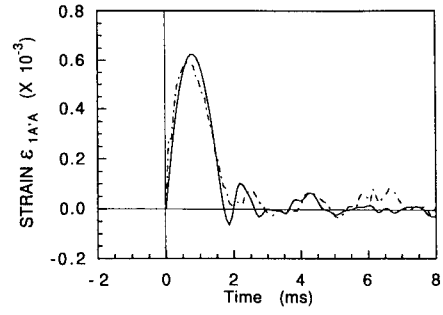

Longitudinal strain

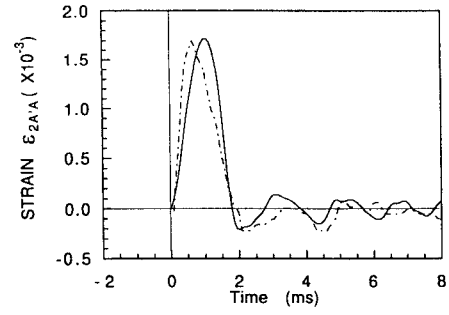

Circumferential strain

Fig. 5 Longitudinal and circumferential strains at point A′ ($X = 0, \Theta = 0, Z = -h/2$) for impact on point A ($X = 0, \Theta = 0, Z = h/2$): –·–·–, experiment and ——, theory.

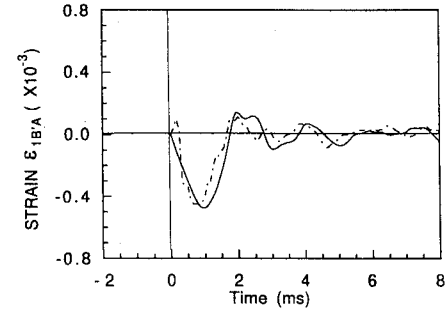

Fig. 6 Longitudinal strain at point B′ ($X = 30, \Theta = 0, Z = -h/2$) for impact on point A ($X = 0, \Theta = 0, Z = h/2$): –·–·–, experiment and ——, theory.

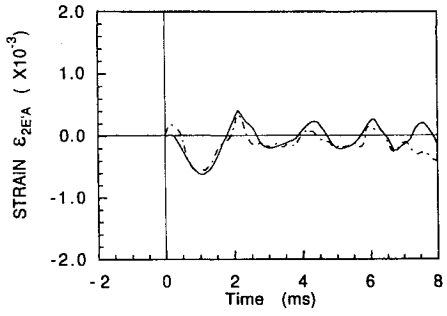

Fig. 7 Circumferential strain at point E′ ($X = 0, \Theta = 30$ deg, $Z = -h/2$) for impact on point A ($X = 0, \Theta = 0, Z = h/2$): -·-·-, experiment and ——, theory.

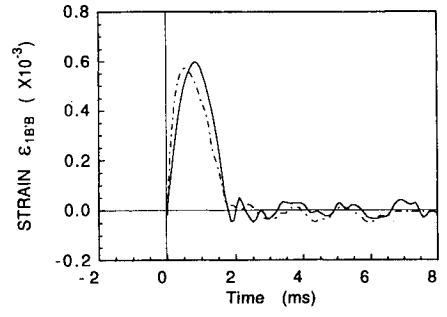

Longitudinal strain

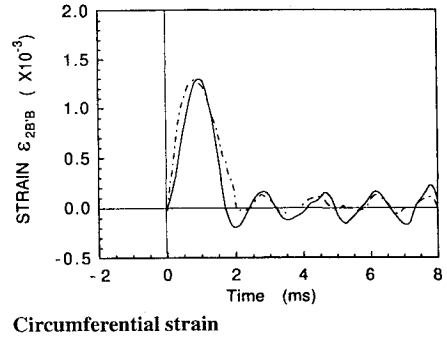

Circumferential strain

Fig. 8 Longitudinal and circumferential strains at point B′ ($X = 30, \Theta = 0, Z = -h/2$) for impact on point B ($X = 30, \Theta = 0, Z = h/2$): -·-·-, experiment and ——, theory.

B. Strain Response to Noncentral Impact

Strain responses excited by noncentral impact were also investigated. This was done by impacting points A, B, C, and D individually (Fig. 3) with a common velocity. The corresponding strain responses at A′, B′, C′, and D′ behind points A, B, C, and D were measured. Figures 5 and 8–10 illustrate the resultant respective longitudinal and circumferential strain responses. The calculated results show good agreement with measurements for all cases, thus verifying that the present solutions for noncentral impact are valid. Figures 5 and 8–10 show that the strain responses at points A′, B′, C′, and D′ induced by impact on points A, B, C, and D exhibit similar behavior; the strains increase during loading, decrease thereafter, and reach a peak approximately midway through the contact duration.

Let ε_{1m} and ε_{2m} represent, respectively, the maximum longitudinal and circumferential strains during impact ($0 < t < T$). The variation of these maximum strains with impact location X is illustrated in Fig. 11. It is observed that ε_{1m} and ε_{2m} decrease with X, the distance from the midpoint of the shell, with both strains exhibiting maximum values at point A′ for impact on A ($X = 0$). This ties in with the fact that point A′ is farthest from the two supported edges and therefore has the greatest structural compliance. It is also observed that ε_{2m} decreases with X much more rapidly than ε_{1m} does. The maximum longitudinal strain at D′ arising from impact on D′ is 67% of the maximum value at point A′ for impact on A. However, the corresponding maximum circumferential strain at D′ is only 25% of the value at A′. This is explained by the fact that at the cylinder edge the simply supported boundary condition requires zero

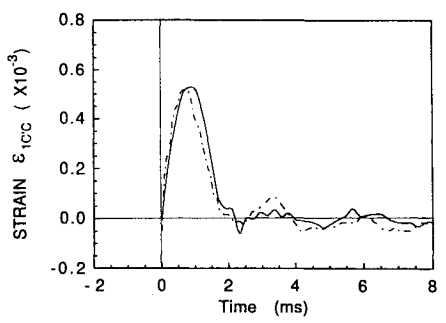

Longitudinal strain

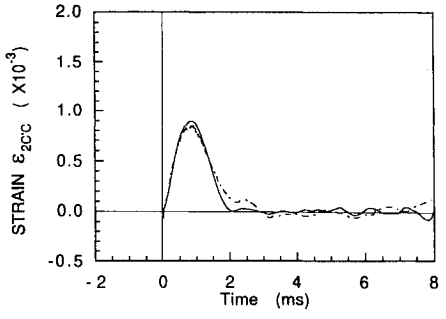

Circumferential strain

Fig. 9 Longitudinal and circumferential strains at point C′ ($X = 60, \Theta = 0, Z = -h/2$) for impact on point C ($X = 60, \Theta = 0, Z = h/2$): -·-·-, experiment and ——, theory.

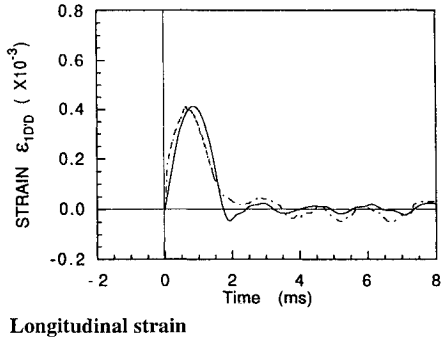

Longitudinal strain

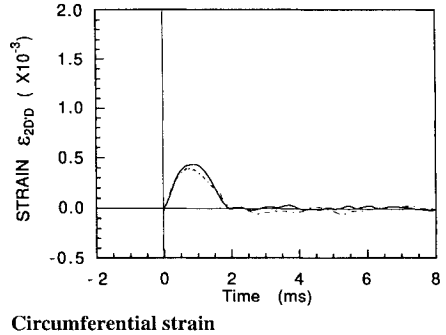

Circumferential strain

Fig. 10 Longitudinal and circumferential strains at point D′ ($X = 90, \Theta = 0, Z = -h/2$) for impact on point D ($X = 90, \Theta = 0, Z = h/2$): -·-·-, experiment and ——, theory.

displacement in the circumferential direction but allows displacement in the longitudinal direction; therefore, the effect of boundary restraint on circumferential stiffness is comparatively larger. This means that near the edges a cylinder exhibits a higher stiffness in the circumferential direction because of end restraints.

C. Strain Distributions During Impact

Longitudinal strain distributions along the inner surface of the shell (for central and noncentral impact) were calculated using Eqs. (21a) and (21b). Figure 12 shows longitudinal strain distributions along the X direction at four instants of time during loading.

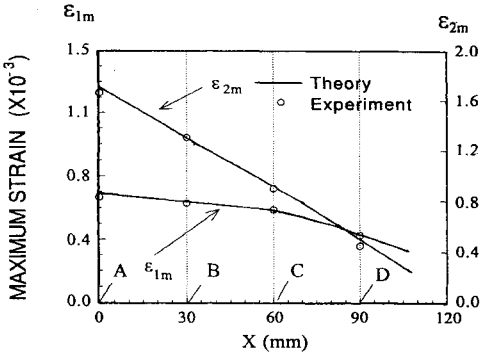

Fig. 11 Maximum strain induced as impact point varies along length of shell.

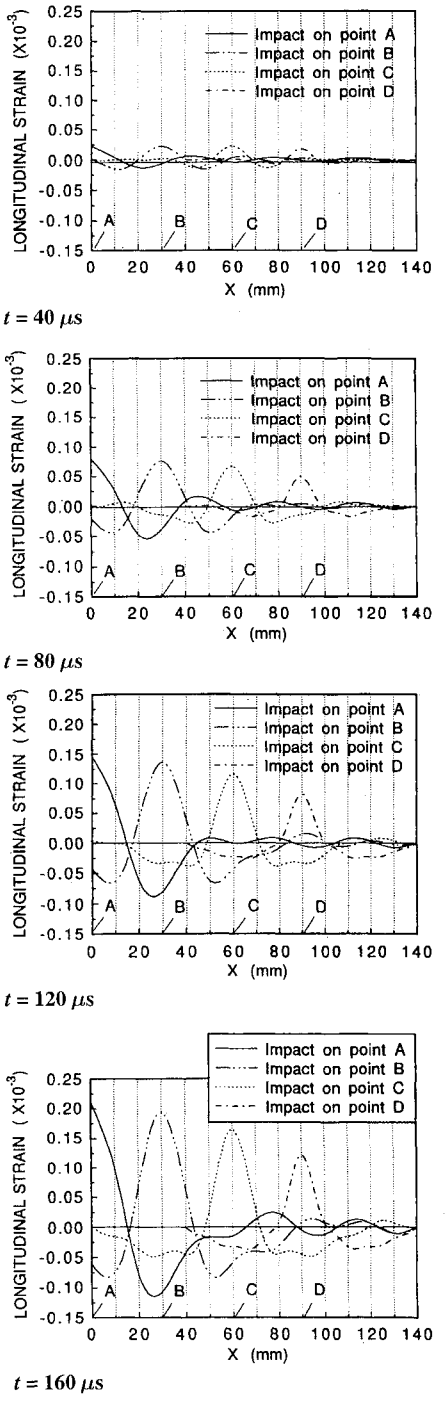

Fig. 12 Longitudinal strain distributions along the X axis on the inner surface of the cylinder from 40 to 160 μs after commencement of contact.

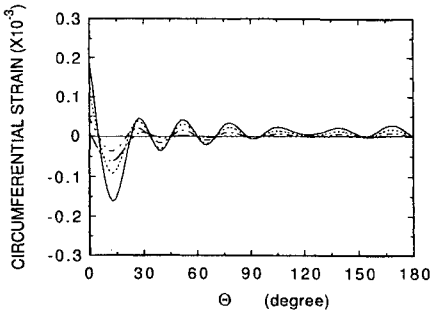

Fig. 13 Circumferential strain distributions along the Θ axis on the inner surface of the cylinder from 40 to 160 μs after commencement of contact: –· · ·–, t = 40 μs; –·–·–, t = 80 μs; ....., t = 120 μs; and ——, t = 160 μs.

At each instant, four strain distributions are plotted, one each for impact at points A, B, C, and D. Inspection of Fig. 12 shows that if the strain distributions corresponding to noncentral impact are shifted to the left, such that the respective points of impact are superimposed onto the center of the cylinder ($X = 0$), all of the strain distributions exhibit a similar profile. Tensile strains initiate, respectively, at points A′, B′, C′, and D′ (behind the impact points A, B, C, and D) and are concentrated around these points. The strains decay rapidly with distance from the respective impact points and become compressive. As time increases, tensile strains around the impact points increase in magnitude. An examination of the longitudinal strain distributions along the X direction shows again that no matter where the shell is impacted, the maximum strain occurs at the impact point.

Figure 13 shows circumferential strain distributions along the Θ direction for four instants of time during loading by central impact (point A). The distribution of circumferential strains in the Θ direction differs slightly from that of longitudinal strains in the X direction. The area of compressive circumferential strain closest to the impact center ($5 < \Theta < 20$ deg) is larger than that of tensile circumferential strain around the impact center ($0 < \Theta < 5$ deg); the magnitude of the maximum compressive strain at $\Theta \approx 13$ deg is only slightly less than that of the maximum tensile strain at point A′ ($\Theta = 0$). These characteristics of the compressive strains in the region $5 < \Theta < 20$ deg arise from curvature [$1/R = (1/0.108)\text{m}^{-1}$] in the Θ direction, which promotes circumferential compression. However, the maximum circumferential strain is still tensile and located at point A′ ($X = 0$, $\Theta = 0$, $Z = -h/2$); therefore, transverse cracks are most likely to be generated in the innermost lamina at the epicenter of the impact.

V. Conclusions

The present analysis facilitates investigation of the transient dynamic response of crossply laminated cylindrical shells impacted by a solid striker with a low velocity at any location. It was employed to examine strains induced in the case of a unidirectional laminated cylindrical shell under central and noncentral impact. An experimental study of impact on the shell was also conducted. Results obtained show that the maximum strains occur during contact ($0 < t < T$). With respect to strain distributions, it is found that no matter where a cylindrical shell is impacted, the maximum longitudinal and circumferential strains occur at (behind) the impact point; for a given impact, the maximum strains are largest for impact at the center of the shell. The results also show that the history and location of the contact force and their relationship to strain magnitudes facilitate determination of the occurrence and location of maximum strains in an impacted shell.

Appendix: Definitions of Operators and Coefficients

The differential operators L_{ij} in Eq. (2) are

$$L_{11} = A_{11}\frac{\partial^2}{\partial x^2} + A_{66}\frac{\partial^2}{R^2\partial\theta^2} - \bar{I}_1\frac{\mathrm{d}^2}{\mathrm{d}t^2}$$

$$L_{12} = L_{21} = (A_{12} + A_{66})\frac{\partial^2}{R\partial x\partial\theta}$$

$$L_{13} = -L_{31} = \frac{A_{11}}{R}\frac{\partial}{\partial x} - \frac{4}{3h^2}\left(E_{11}\frac{\partial^3}{\partial x^3} + E_{12}\frac{\partial^3}{R^2\partial x\partial\theta^2} + 2E_{66}\frac{\partial^3}{R^2\partial x\partial\theta^2}\right) + \bar{I}_3\frac{\partial}{\partial x_1}\left(\frac{\mathrm{d}^2}{\mathrm{d}t^2}\right)$$

$$L_{14} = L_{41} = B_{11}\frac{\partial^2}{\partial x^2} + B_{66}\frac{\partial^2}{R^2\partial\theta^2} - \frac{4}{3h^2}\left(E_{11}\frac{\partial^2}{\partial x^2} + E_{66}\frac{\partial^2}{R^2\partial\theta^2}\right) - \bar{I}_2\frac{\mathrm{d}^2}{\mathrm{d}t^2}$$

$$L_{15} = L_{51} = (B_{12} + B_{66})\frac{\partial^2}{R\partial x\partial\theta} - \frac{4}{3h^2}(E_{12} + E_{66})\frac{\partial^2}{R\partial x\partial\theta}$$

$$L_{22} = A_{66}\frac{\partial^2}{\partial x^2} + A_{22}\frac{\partial^2}{R^2\partial\theta^2} - \bar{I}_1'\frac{\mathrm{d}^2}{\mathrm{d}t^2}$$

$$L_{23} = -L_{32} = \frac{A_{12}}{R^2}\frac{\partial}{\partial\theta} - \frac{4}{3h^2}\left(E_{22}\frac{\partial^3}{R^3\partial\theta^3} + E_{12}\frac{\partial^3}{R\partial x^2\partial\theta} + 2E_{66}\frac{\partial^3}{R\partial x^2\partial\theta}\right) + \bar{I}_3'\frac{\partial}{R\partial\theta}\left(\frac{\mathrm{d}^2}{\mathrm{d}t^2}\right)$$

$$L_{24} = L_{42} = L_{15}$$

$$L_{25} = L_{52} = B_{66}\frac{\partial^2}{\partial x^2} + B_{22}\frac{\partial^2}{R^2\partial\theta^2} - \frac{4}{3h^2}\left(E_{66}\frac{\partial^2}{\partial x^2} + E_{22}\frac{\partial^2}{R^2\partial\theta^2}\right) - \bar{I}_2'\frac{\mathrm{d}^2}{\mathrm{d}t^2}$$

$$L_{33} = A_{55}\frac{\partial^2}{\partial x^2} + A_{44}\frac{\partial^2}{R^2\partial\theta^2} - \frac{A_{22}}{R^2} - \frac{16}{9h^4}H_{11}\frac{\partial^4}{\partial x^4} - \frac{\lambda_1^2}{9}H_{22}\frac{\partial^4}{R^4\partial\theta^4} - \frac{32}{9h^4}(H_{12} + 2H_{66})\frac{\partial^4}{R^2\partial x^2\partial\theta^2} - \frac{4}{h^2}\left(2D_{55} - \frac{4}{h^2}F_{55} - \frac{2E_{12}}{3R}\right)\frac{\partial^2}{\partial x^2} - \frac{4}{h^2}\left(2D_{44} - \frac{4}{h^2}F_{44} - \frac{2E_{22}}{3R}\right)\frac{\partial^2}{R^2\partial\theta^2} + \frac{16}{9h^4}I_7\left[\frac{\partial^2}{\partial x^2}\left(\frac{\mathrm{d}^2}{\mathrm{d}t^2}\right) + \frac{\partial^2}{R^2\partial\theta^2}\left(\frac{\mathrm{d}^2}{\mathrm{d}t^2}\right)\right] \tag{A1}$$

$$L_{34} = -L_{43} = \left(A_{55} - \frac{B_{12}}{R}\right)\frac{\partial}{\partial x} + \frac{4}{3h^2}\left(F_{11} - \frac{4}{3h^2}H_{11}\right)\frac{\partial^3}{\partial x^3} + \frac{4}{3h^2}(F_{12} + 2F_{66})\frac{\partial^3}{R^2\partial x\partial\theta^2} - \frac{16}{9h^2}(H_{12} + 2H_{66})\frac{\partial^3}{R^2\partial x\partial\theta^2} + \frac{4}{3h^2}\frac{E_{12}}{R}\frac{\partial}{\partial x} - \frac{4}{h}\left(2D_{55} - \frac{4}{h}F_{55}\right)\frac{\partial}{\partial x} - \bar{I}_5\frac{\partial}{\partial x}\left(\frac{\mathrm{d}^2}{\mathrm{d}t^2}\right)$$

$$L_{35} = -L_{53} = \left(A_{44} - \frac{B_{22}}{R}\right)\frac{\partial}{R\partial\theta} + \frac{4}{3h^2}\left(F_{22} - \frac{4}{3h^2}H_{22}\right)\times\frac{\partial^3}{R^3\partial\theta^3} + \frac{4}{3h^2}(F_{12} + 2F_{66})\frac{\partial^3}{R\partial x^2\partial\theta} - \frac{16}{9h^4}(H_{12} + 2H_{66})\frac{\partial^3}{R\partial x^2\partial\theta} + \frac{4}{3h^2}\frac{E_{22}}{R}\frac{\partial}{\partial\theta} - \frac{4}{h^2}\left(2D_{44} - \frac{4}{h^2}F_{44}\right)\frac{\partial}{R\partial\theta} - \bar{I}_5\frac{\partial}{R\partial\theta}\left(\frac{\mathrm{d}^2}{\mathrm{d}t^2}\right)$$

$$L_{44} = D_{11}\frac{\partial^2}{\partial x^2} + D_{66}\frac{\partial^2}{R^2\partial\theta^2} - A_{55} - \frac{4}{3h^2}\left(2F_{11} - \frac{4}{3h^2}H_{11}\right)\times\frac{\partial^2}{\partial x^2} - \frac{4}{3h^2}\left(2F_{66} - \frac{4}{3h^2}H_{66}\right)\frac{\partial^2}{R^2\partial\theta^2} + \frac{8}{h^2}D_{55} - \frac{16}{h^4}F_{55} - \bar{I}_4\frac{\mathrm{d}^2}{\mathrm{d}t^2}$$

$$L_{45} = L_{54} = (D_{12} + D_{66})\frac{\partial^2}{R\partial x\partial\theta} - \left[\frac{8}{3h^2}(F_{12} + F_{66}) - \frac{16}{9h^4}(H_{12} + H_{66})\right]\frac{\partial^2}{R\partial x\partial\theta}$$

$$L_{55} = D_{66}\frac{\partial^2}{\partial x^2} + D_{22}\frac{\partial^2}{R^2\partial\theta^2} - A_{44} - \frac{4}{3h^2}\times\left(2F_{66} - \frac{4}{3h^2}H_{66}\right)\frac{\partial^2}{\partial x^2} - \frac{4}{3h^2}\left(2F_{22} - \frac{4}{3h^2}H_{22}\right)\frac{\partial^2}{R^2\partial\theta^2} + \frac{8}{h^2}D_{44} - \frac{16}{h^4}F_{44} - \bar{I}_4\frac{\mathrm{d}^2}{\mathrm{d}t^2}$$

where the laminate stiffness constants A_{ij}, B_{ij}, D_{ij}, E_{ij}, F_{ij}, and H_{ij} are given by

$$(A_{ij}, B_{ij}, D_{ij}, E_{ij}, F_{ij}, H_{ij}) = \sum_{k=1}^{L}\int_{z_{k-1}}^{z_k} Q_{ij}^{(k)}(1, z, z^2, z^3, z^4, z^6)\,\mathrm{d}z \tag{A2}$$

where $(i, j = 1, 2, 4, 5, 6)$ and $Q_{ij}^{(k)}$ are the transformed stiffness constants in the shell coordinate system, and the inertia factors $\bar{I}_i$ and $\bar{I}_i'$ are defined by Ref. 9.

The coefficients T_{ij} in Eq. (10) are

$$T_{11} = -A_{11}M^2 - A_{66}N^2$$

$$T_{12} = T_{21} = -(A_{12} + A_{66})MN$$

$$T_{13} = T_{31} = -(A_{12}/R)M - (4/3h^2)M\left(E_{11}M^2 + E_{12}N^2 + 2E_{66}N^2\right)$$

$$T_{14} = T_{41} = -B_{11}M^2 - B_{66}N^2 + (4/3h^2)\left(E_{12}M^2 + E_{66}N^2\right)$$

$$T_{15} = T_{51} = -(B_{12} + B_{66})MN + (4/3h^2)(E_{12} + E_{66})MN$$

$$T_{22} = -A_{66}M^2 - A_{22}N^2$$

$$T_{23} = T_{32} = -[(A_{12}/R_1) + (A_{22}/R_2)]N - (4/3h^2)N\left(E_{22}N^2 + E_{12}M^2 + 2E_{66}M^2\right)$$

$$T_{24} = T_{42} = T_{15}$$

$$T_{25} = T_{52} = -B_{66}M^2 - B_{22}N^2 + (4/3h^2)\left(E_{66}M^2 + E_{22}N^2\right)$$

$$T_{33} = -A_{55}M^2 - A_{44}N^2 - \frac{A_{22}}{R^2} - \frac{16}{9h^4}H_{11}M^4 - \frac{16}{9h^4}H_{22}N^4 - \frac{32}{9h^4}(H_{12} + 2H_{66})M^2N^2 + \frac{4}{h^2}\left(2D_{55} - \frac{4}{h^2}F_{55} - \frac{2E_{12}}{3R}\right)M^2 + \frac{4}{h^2}\left(2D_{44} - \frac{4}{h^2}F_{44} - \frac{2E_{22}}{3R}\right)N^2$$

$$T_{34} = T_{43} = \left(A_{55} - \frac{B_{12}}{R}\right)M - \frac{4}{3h^2}\left(F_{11} - \frac{4}{3h^2}H_{11}\right)M^3 - \frac{4}{3h^2}(F_{12} + 2F_{66})MN^2 + \frac{16}{9h^4}(H_{12} + 2H_{66})MN^2 + \frac{4}{3h^2}\frac{E_{12}}{R}M - \frac{4}{h^2}\left(2D_{55} - \frac{4}{h^2}F_{55}\right)M$$

$$T_{35} = T_{53} = \left(A_{44} - \frac{B_{22}}{R}\right)N - \frac{4}{3h^2}\left(F_{22} - \frac{4}{3h^2}H_{22}\right)N^3$$
$$- \frac{4}{3h^2}(F_{12} + 2F_{66})M^2N + \frac{16}{9h^4}(H_{12} + 2H_{66})M^2N \qquad \text{(A3)}$$
$$+ \frac{4}{3h^2}\left(\frac{E_{12}}{R_1} + \frac{E_{22}}{R_2}\right)N - \frac{4}{h^2}\left(2D_{44} - \frac{4}{h^2}F_{44}\right)N$$

$$T_{44} = -D_{11}M^2 - D_{66}N^2 - A_{55} + \frac{4}{3h^2}\left(2F_{11} - \frac{4}{3h^2}H_{11}\right)M^2$$
$$+ \frac{4}{3h^2}\left(2F_{66} - \frac{4}{3h^2}H_{66}\right)N^2 + \frac{8}{h^2}D_{55} - \frac{16}{h^4}F_{55}$$

$$T_{45} = T_{54} = -(D_{12} + D_{66})MN$$
$$+ \left[\frac{8}{3h^2}(F_{12} + F_{66}) - \frac{16}{9h^4}(H_{12} + H_{66})\right]MN$$

$$T_{55} = -D_{66}M^2 - D_{22}N^2 - A_{44} + \frac{4}{3h^2}\left(2F_{66} - \frac{4}{3h^2}H_{66}\right)M^2$$
$$+ \frac{4}{3h^2}\left(2F_{22} - \frac{4}{3h^2}H_{22}\right)N^2 + \frac{8}{h^2}D_{44} - \frac{16}{h^4}F_{44}$$

where $M = m\xi^*\pi/L$ and $N = n/R$.

References

[1]Sun, C. T., and Chattopadhyay, S., "Dynamic Response of Anisotropic Laminated Plates Under Initial Stress due to Impact of a Mass," *Journal of Applied Mechanics*, Vol. 43, Sept. 1975, pp. 693–698.

[2]Dobyns, A. L., "Analysis of Simply Supported Orthotropic Plates Subject to Static and Dynamic Loads," *AIAA Journal*, Vol. 19, No. 5, 1981, pp. 642–650.

[3]Whitney, J. M., and Pagano, N. J., "Shear Deformation in Heterogeneous Anisotropic Plates," *Journal of Applied Mechanics*, Vol. 37, Dec. 1970, pp. 1031–1036.

[4]Ramkumar, R. L., and Thakar, Y. R., "Dynamic Response of Curved Laminated Plates Subjected to Low Velocity Impact," *Journal of Engineering Materials and Technology*, Vol. 109, Jan. 1987, pp. 67–71.

[5]Christoforou, A. P., and Swanson, S. R., "Analysis of Simply-Supported Orthotropic Cylindrical Shells Subject to Lateral Impact Loads," *Journal of Applied Mechanics*, Vol. 57, June 1990, pp. 376–382.

[6]Bert, C. W., and Birman, V., "Parametric Instability of Thick, Orthotropic, Circular Cylindrical Shells," *Acta Mechanica*, Vol. 71, Feb. 1988, pp. 67–76.

[7]Gong, S. W., Toh, S. L., and Shim, V. P. W., "The Elastic Response of Orthotropic Laminated Cylindrical Shells to Low Velocity Impact," *Composites Engineering*, Vol. 4, No. 2, 1994, pp. 247–266.

[8]Gong, S. W., Shim, V. P. W., and Toh, S. L., "Impact Response of Laminated Shells with Orthogonal Curvatures," *Composites Engineering*, Vol. 5, No. 3, 1995, pp. 257–275.

[9]Reddy, J. N., and Liu, C. F., "A Higher-Order Shear Deformation Theory of Laminated Elastic Shells," *International Journal of Engineering Science*, Vol. 23, No. 3, 1985, pp. 319–330.

[10]Gong, S. W., "A Study of Impact on Composite Laminated Shells," Ph.D. Dissertation, Dept. of Mechanical and Production Engineering, National Univ. of Singapore, Singapore, 1995.

[11]Anon., "Standard Test Method for Tensile Properties of Fiber-Resin Composites," *ASTM Standards and Literature References for Composite Materials*, edited by R. A. Storer, 1st ed., American Society for Testing and Materials, ASTM D3039-76, 1987, pp. 35–40.

[12]Timoshenko, S. P., and Goodier, J. N., *Theory of Elasticity*, McGraw–Hill, New York, 1970.

10,000 copies sold!

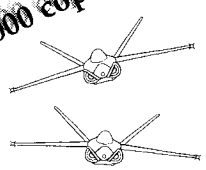

"The addition of the computer disk should greatly enhance the value of this text. The text is a one-of-a-kind resource for teaching a modern aircraft design course."
J.F. Marchman, Virginia Institute of Technology

Aircraft Design: A Conceptual Approach Second Edition
Daniel P. Raymer

Now you get everything that made the first edition a classic and more. *Aircraft Design: A Conceptual Approach* fills the need for a textbook in which both aircraft analysis and design layout are covered equally, and the interactions between these two aspects of design are explored in a manner consistent with industry practice. New to this edition: Production methods, post stall maneuver, VTOL, engine cycle analysis, plus a complete design example created for use with RDS-STUDENT.

1992, 739 pp, illus, Hardback
ISBN 0-930403-51-7
AIAA Member $53.95, Nonmembers $66.95
Order #: 51-7(945)

RDS-STUDENT: Software for Aircraft Design, Sizing, and Performance Version 3.0
Daniel P. Raymer

A powerful new learning tool, RDS-STUDENT lets students apply everything they learn—as they learn it. The software package includes comprehensive modules for aerodynamics, weights, propulsion, aircraft data file, sizing and mission analysis, cost analysis, design layout, and performance analysis, including takeoff, landing, rate of climb, P_s, f_s, turn rate and accelertion. RDS-STUDENT also provides graphical output for drag polars, L/D ratio, thrust curves, flight envelope, range parameter, and other data.

1992, 71 pp User's Guide and 3.5" disk
ISBN 1-56347-047-0
AIAA Members $54.95, Nonmembers $69.95
Order #: 47-0(945)

Buy Both and Save!
Aircraft Design, 2nd Edition and RDS-STUDENT
AIAA Members $95.95, Nonmembers $125.95
Order #: 51-7/47-0(945)

Place your order today! Call 1-800/682-AIAA

AIAA
American Institute of Aeronautics and Astronautics
Publications Customer Service, 9 Jay Gould Ct., P.O. Box 753, Waldorf, MD 20604
FAX 301/843-0159 Phone 1-800/682-2422 8 a.m. - 5 p.m. Eastern

Sales Tax: CA residents, 8.25%; DC, 6%. For shipping and handling add $4.75 for 1-4 books (call for rates for higher quantities). Orders under $100.00 must be prepaid. Foreign orders must be prepaid and include a $25.00 postal surcharge. Please allow 4 weeks for delivery. Prices are subject to change without notice. Returns will be accepted within 30 days. Non-U.S. residents are responsible for payment of any taxes required by their government.